Revealing Henle's Fiber Layer Using Spectral Domain Optical Coherence Tomography

Brandon J. Lujan,[1,2] *Austin Roorda,*[1] *Robert W. Knighton,*[3] *and Joseph Carroll*[4,5,6]

Purpose. Spectral domain optical coherence tomography (SD-OCT) uses infrared light to visualize the reflectivity of structures of differing optical properties within the retina. Despite their presence on histologic studies, traditionally acquired SD-OCT images are unable to delineate the axons of photoreceptor nuclei, Henle's fiber layer (HFL). The authors present a new method to reliably identify HFL by varying the entry position of the SD-OCT beam through the pupil.

Methods. Fifteen eyes from 11 subjects with normal vision were prospectively imaged using 1 of 2 commercial SD-OCT systems. For each eye, the entry position of the SD-OCT beam through the pupil was varied horizontally and vertically. The reflectivity of outer retinal layers was measured as a function of beam position, and thicknesses were recorded.

Results. The reflectivity of HFL was directionally dependent and increased with eccentricity on the side of the fovea opposite the entry position. When HFL was included in the measurement, the thickness of the outer nuclear layer (ONL) of central horizontal B-scans increased by an average of 52% in three subjects quantified. Four cases of pathology, in which alterations to the normal macular geometry affected HFL intensity, were identified.

Conclusions. The authors demonstrated a novel method to distinguish HFL from true ONL. An accurate measurement of the ONL is critical to clinical studies measuring photoreceptor layer thickness using any SD-OCT system. Recognition of the optical properties of HFL can explain reflectivity changes imaged in this layer in association with macular pathology. (*Invest Ophthalmol Vis Sci.* 2011;52:1486–1492) DOI:10.1167/iovs.10-5946

Henle's fiber layer (HFL) contains bundles of unmyelinated cone and rod photoreceptor axons terminating in the pedicles and spherules that synapse in the retinal outer plexiform layer (OPL).[1] These fibers are intermingled with Müller cell processes and are obliquely oriented as a result of foveal pit development where photoreceptors migrate inward and ganglion cells migrate outward.[2,3] Like axons elsewhere in the central nervous system, the axons of HFL contain microtubules and are long, cylindrical structures.[1–3] Their average length is 558 μm,[4] and the first synapses occur with dendrites of bipolar and horizontal cells approximately 350 μm from the foveal center.[4] Given the large number of central foveal photoreceptor nuclei and this marked displacement, HFL constitutes a significant fraction of the thickness of retinal layers within the macula, as is evident histologically (Fig. 1). HFL is oriented radially about the fovea and is indirectly visible ophthalmoscopically in patients with macular star formation in neuroretinitis.[5] HFL also demonstrates the optical property of form birefringence, a property that can be exploited to infer the location of the foveal center as a direct consequence of its consistent effects on polarized light.[6]

Optical coherence tomography (OCT) uses infrared light to interferometrically derive optical reflectivity information varying by depth in living tissues.[7] The use of broadband light sources, a spectrometer, and the application of signal processing techniques has culminated in commercial spectral domain (SD) OCT systems that are capable of imaging with a 5-μm axial resolution in retinal tissue.[8,9] These improvements, along with acquisition speeds fast enough to permit frame averaging without significant motion artifact, contribute to improved image quality in SD-OCT devices capable of identifying structures that could not previously be resolved.[10]

Despite advances in SD-OCT hardware and software, HFL visualization has remained elusive. A seminal paper published in 2004 comparing in vitro OCT images of monkey fovea to histology recognized HFL as a major layer of the retina that could be visualized in vitro and that should be accounted for in vivo.[11] However, since that publication, HFL has not been included in diagrams of retinal layers visualized by OCT, likely because of the inability to distinguish a change in reflectivity at the interface between the HFL and the outer nuclear layer (ONL).[12–14] Furthermore, segmentation algorithms, normative thickness data, and ONL measurements overlying drusen have recently been published that do not recognize the contribution to macular thickness provided by HFL to the ONL.[15–19] Although the need to account for the presence of HFL in OCT images has recently been recognized, the proposed means to measure the contribution of the HFL was an inferential normative model based on high-quality pathologic specimens rather than by a direct means of visualization (Curcio CA, et al. *IOVS*. 2010;51:ARVO E-Abstract 2286). The only explicit mention of the optical conditions in which HFL may be visualized with OCT can be found in a letter to the editor and was not experimentally validated.[20] In our study we describe a systematic method that can be applied to commercial SD-OCT systems to *directly* visualize and quantify HFL. Additionally, we provide an optical explanation of this phenomenon and demonstrate its clinical relevance.

From the [1]Department of Vision Science, School of Optometry, University of California, Berkeley, California; the [2]West Coast Retina Medical Group, San Francisco, California; the [3]Bascom Palmer Eye Institute, University of Miami, Miller School of Medicine, Miami, Florida; and the Departments of [4]Ophthalmology, [5]Cell Biology, Neurobiology, and Anatomy, and [6]Biophysics, Medical College of Wisconsin, Milwaukee, Wisconsin.

Presented in part at the annual meeting of the Association for Research in Vision and Ophthalmology, Fort Lauderdale, Florida, May 2010.

Supported by National Institutes of Health Grants K12 EY017269 (BJL), EY014375 (AR), P30EY001931 (JC) and R01EY017607 (JC); an unrestricted departmental grant and a Career Development Award from Research to Prevent Blindness (JC); and the Thomas M. Aaberg Sr. Retina Research Fund (JC).

Submitted for publication May 25, 2010; revised September 2, 2010; accepted October 5, 2010.

Disclosure: **B.J. Lujan**, Carl Zeiss Meditec, Inc. (F); **A. Roorda**, Carl Zeiss Meditec, Inc. (F); **R.W. Knighton,** Carl Zeiss Meditec, Inc. (C); **J. Carroll**, None

Corresponding author: Brandon J. Lujan, Roorda Laboratory, 485 Minor Hall, Berkeley, CA 94720; blujan@berkeley.edu.

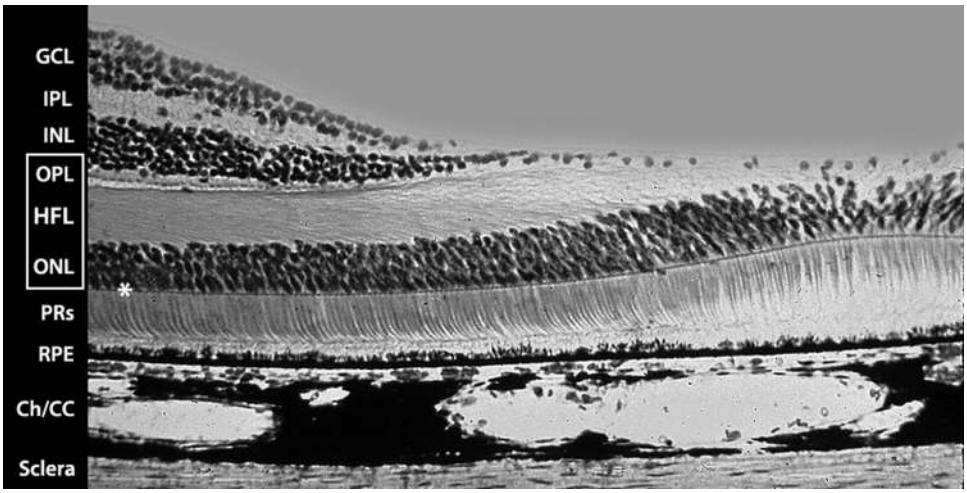

FIGURE 1. Mammalian foveal histology, courtesy of Roger C. Wagner, Professor Emeritus of Biological Sciences, University of Delaware, http://dspace.udel.edu:8080/dspace/handle/19716/1884. Photoreceptor components are indicated by the *rectangle*, showing the substantial contributions by the photoreceptor inner and outer segments, nuclei, and axons running in HFL. GCL, ganglion cell layer; PRs, photoreceptor IS and OS; Ch/CC, choriocapillaris and choroid. *ELM.

MATERIALS AND METHODS

Data Collection

All subjects provided informed consent to participate in this study. This study was approved by Institutional Review Boards at the University of California at Berkeley and the Medical College of Wisconsin, and the study protocol followed the tenets of the Declaration of Helsinki.

One or both eyes of each subject were dilated using 2.5% phenylephrine and 1% tropicamide. Two commercially available SD-OCT systems were used to collect data for this study. Twelve eyes of eight subjects and two eyes of two patients with macular disease were imaged using Cirrus HD-OCT (Carl Zeiss Meditec, Inc., Dublin, CA) by the same operator (BJL), and three eyes of three subjects were imaged using a single Bioptigen SD-OCT (Bioptigen, Durham, NC) by a single operator (JC). All scans for a given subject were performed during a single session. The specific protocols for each device are described. Additionally, a retrospective review of two clinical cases obtained using Bioptigen SD-OCT was also performed.

Subjects ranged from 20 to 43 years of age and had refractive errors ranging from a spherical equivalent of +0.50 to −4.50 diopters. SD-OCT data were reviewed, and each included eye defined as normal was determined to be free of macular pathology by a retinal specialist.

The Cirrus HD-OCT is an SD-OCT device that uses a 50-nm bandwidth light source centered at 840 nm, has a 5-μm axial resolution, and obtains 27,000 axially oriented scans (A-scans) per second. Cirrus data are acquired over a 20° field (6 mm for an emmetropic eye) and has a scan depth of 2 mm. Two standard Cirrus scan protocols were used to acquire data—a 512 × 128 cube and a frame-averaged cross-sectional scan through the fovea. The 512 × 128 cube consisted of 128 cross-sectional images, or B-scans, that were each composed of 512 A-scans. The frame-averaged cross-sectional scans were obtained using the system's commercial software (version 4.5), which averages 20 individual B-scans each consisting of 1024 A-scans where the nominal spacing between scans was set to zero. The rendered B-scans have an aspect ratio of 2:1 (i.e., the scale is doubled in the axial dimension), but this was corrected to 1:1 before data analysis described below.

Cirrus SD-OCT has a dedicated pupil camera that permits live monitoring of the pupil position during scans and that indicates the entry position of the SD-OCT beam. This was used in conjunction with B-scans rendered in real time to obtain a beam entry position in which both the horizontal and the vertical B-scans appeared "flat" (i.e., symmetric about the fovea.) Subsequently, the entrance pupil was displaced at multiple intervals superiorly, inferiorly, temporally, and nasally. At each entrance pupil location, a horizontal and vertical frame averaged cross-sectional scan was obtained. The absolute beam entry position was documented using the pupil camera.

The Bioptigen SD-OCT used a 186.3-nm bandwidth centered at 878.4 nm, had a theoretical 1.4-μm axial resolution, and obtained 20,000 A-scans per second. Forty B-scans centered on the fovea, each consisting of 1000 A-scans, were registered and averaged as previously described.[21] A headrest was used to stabilize subjects, and deviation of the entry position from where the B-scan appeared flat was measured using markings on the stage. Additionally, video was recorded of live vertical translation of the stage while vertically oriented B-scans were acquired.

Foveal fixation was confirmed by the midpoint position of the foveal center in each analyzed B-scan. Scans that demonstrated low signal strength or reduced image quality through frame averaging were excluded. Volumetric data sets were evaluated immediately after acquisition and were repeated if motion artifacts were present.

Statistical Analysis

Cirrus B-scans were exported as bitmaps and analyzed using graphics editing software (Photoshop CS4; Adobe Systems, Inc., San Jose, CA) and ImageJ software (developed by Wayne Rasband, National Institutes of Health, Bethesda, MD; available at http://rsb.info.nih.gov/ij/index.html). B-scan intensities were linearly normalized to assign the brightest pixel a value of white and the darkest pixel a value of black.

Measuring HFL Thickness

Horizontal frame-averaged B-scans acquired with Cirrus at the two extreme horizontal entrance positions were used to measure the contribution of different zones of reflectivity between the external limiting membrane (ELM) and the inner plexiform layer (IPL) in five right eyes. Specifically, the side of the B-scan that allowed full visualization of the transition to the outer plexiform layer (OPL) was used for this analysis where the inner segment/outer segment (IS/OS) was 1 mm from the foveal center. The distance from the ELM to the posterior edge of the OPL and the distance from the ELM to the edge of the observed hyporeflective zone within this layer was measured along a line perpendicular to the IS/OS. The relative contribution of this hyporeflective zone corresponding to HFL was reported as a percentage of the total distance between the ELM and the OPL.

Frame-averaged B-scans obtained with Bioptigen from each subject were exported to Image J, where a manual tool was used to segment the images collected at each of three pupil entry positions (nasal, center, temporal). Segmented layer data were processed through custom computing software (MatLab; MathWorks, Natick, MA) to determine the thickness between the ELM and the outer edge of the OPL at each eccentricity and between the ELM and the hyporeflective layer corresponding to HFL.

Measuring Dependence of HFL Reflectance on SD-OCT Scan Angle

Cirrus data were analyzed to assess the relative intensity of HFL as a function of pupil entry positioned in six normal left eyes. The axial

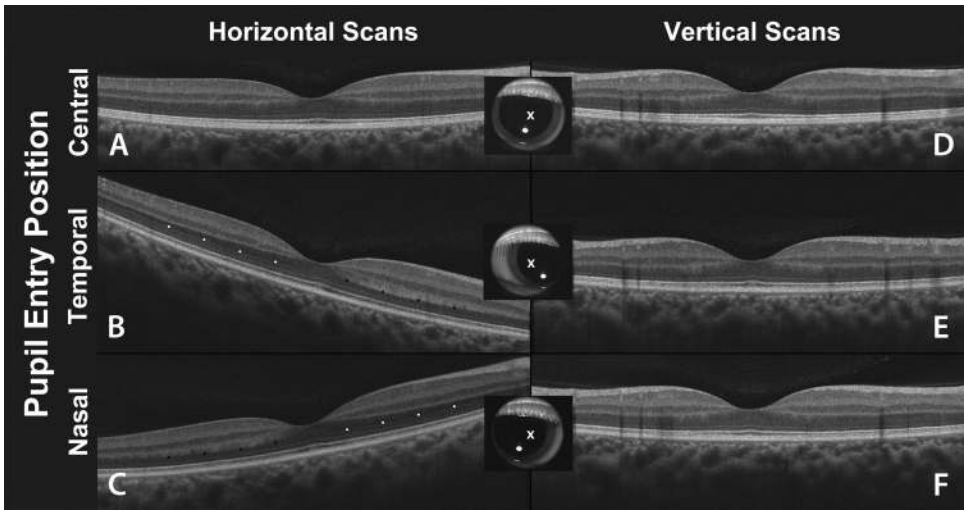

FIGURE 2. The effects of horizontally varying pupil entry position on horizontal and vertical B-scans in a right eye. (**A**) Central entry position with flat B-scans and poor visualization of HFL. Pupil entry position is noted by *central white x*, not the inferior corneal reflection. (**B**) Temporal displacement of the entry beam. Although the foveal anatomy has not changed, there is an apparent tilt to the horizontal B-scan because of unequal optical path lengths (see Fig. 6). A temporal entry position results in hyperreflectivity of HFL relative to the ONL nasal to the fovea (*black dots*) and hyporeflectivity of HFL temporal to the fovea (*white dots*), where distinct demarcations among the ONL, HFL, and IPL are apparent. (**C**) Nasal displacement of the entry beam showing the opposite effects of **B**. (**D–F**) Vertical scans at each pupil entry position show only minimal HFL reflectivity changes and no tilt because vertically the optical path lengths remain equal despite horizontal translation.

magnification of rendered Cirrus B-scans was corrected to display true anatomic dimensions. The foveal center was defined as the point along the photoreceptor IS/OS junction that was the greatest distance away from the RPE along a line normal to the RPE. The angle between the RPE and horizontal was measured 1 mm nasally and 1 mm temporally to the foveal center on each B-scan along the horizontal meridian, with a positive angle corresponding to a clockwise tilt. In each of these B-scans, the average intensity and standard deviations of pixels contained within a 500 × 20-μm rectangle were measured. The rectangle was oriented such that the long axis was parallel to the RPE. It was centered horizontally 1 mm away from the fovea in both nasal and temporal directions and was centered vertically within the inner aspect of the region between the ELM and the OPL corresponding to HFL. Additionally, pixels contained within the same-sized rectangle were obtained from the IPL anterior to the location of the first measurement. The variance of IPL measurements with the pupil entry position was found to be negligible; consequently, these served as a normalization value against changes in incident intensity.

RESULTS

Movement of the SD-OCT beam entrance position horizontally across the pupil was found to result in an apparent tilt of horizontally acquired B-scans and resulted in a reflectivity change corresponding anatomically to HFL. The alteration of HFL reflectivity could be visualized on individual central horizontal B-scans of the 512 × 128 cube, but frame-averaged B-scans augmented the effect through an improved signal-to-noise ratio (Fig. 2). Changing the horizontal entry positions while acquiring vertical B-scans did not result in any change of reflectivity in the HFL, nor did it result in an apparent tilting of the scan. Conversely, vertical translation of the beam entrance position resulted in apparent tilting of vertically acquired B-scans (Supplementary Movie S1, http://www.iovs.org/lookup/suppl/doi:10.1167/iovs.10-5946/-/DCSupplemental) but not of horizontally acquired B-scans (data not shown).

The position of the entrance beam could be determined by the pupil camera on Cirrus scans. As the beam entry position was moved, there was a corresponding change in the apparent tilt of the B-scan. In several cases, the geometric center of the pupil did not correspond to the entry position, yielding a flat B-scan. Changes in beam entry position in the direction of the scan could also be determined directly by monitoring the tilt of the B-scan relative to the axially oriented direction of A-scans, most notably by the hyporeflectivity deep to retinal blood vessels. This was found to be a more precise means of determining pupil entry position than relying on the pupil camera, where image distortions increased the likelihood of registration errors.

Movement toward the nasal pupil resulted in a tilt of the B-scan such that the macula temporal to the fovea appeared lower in the scan than the macula nasal to the fovea. Concurrently, the intensity of pixels corresponding to the temporal HFL increased, whereas the nasal HFL decreased in intensity. The pixel values corresponding to HFL were normalized by the IPL because the intensity from HFL could be altered not only by the intrinsic reflectivity of the tissue but also by variations of incident intensity of the scan given the variable ocular transmission and scatter. The IPL intensity values were found to have a mean coefficient of variation of 6% across subjects. Given that SD-OCT images are rendered on a logarithmic scale, this was extremely invariant compared with HFL, where the mean coefficient of variation was 27% across subjects. Normalization by the IPL resulted in a direct relationship between scan angle and HFL intensity and demonstrated its directional reflectance properties (Fig. 3). Reflectivity of the nasal macula in-

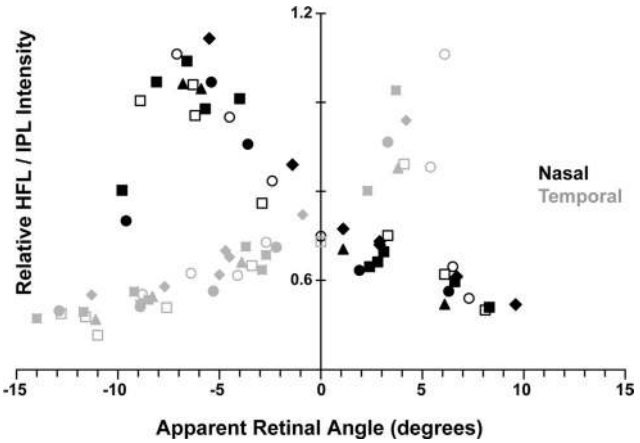

FIGURE 3. Relative intensities of HFL reflectivity normalized by the IPL reflectivity compared with the retinal angle measured 1 mm away from the foveal center in six left eyes. Different symbols represent individual subjects in nasal (*black*) and temporal (*gray*) macula.

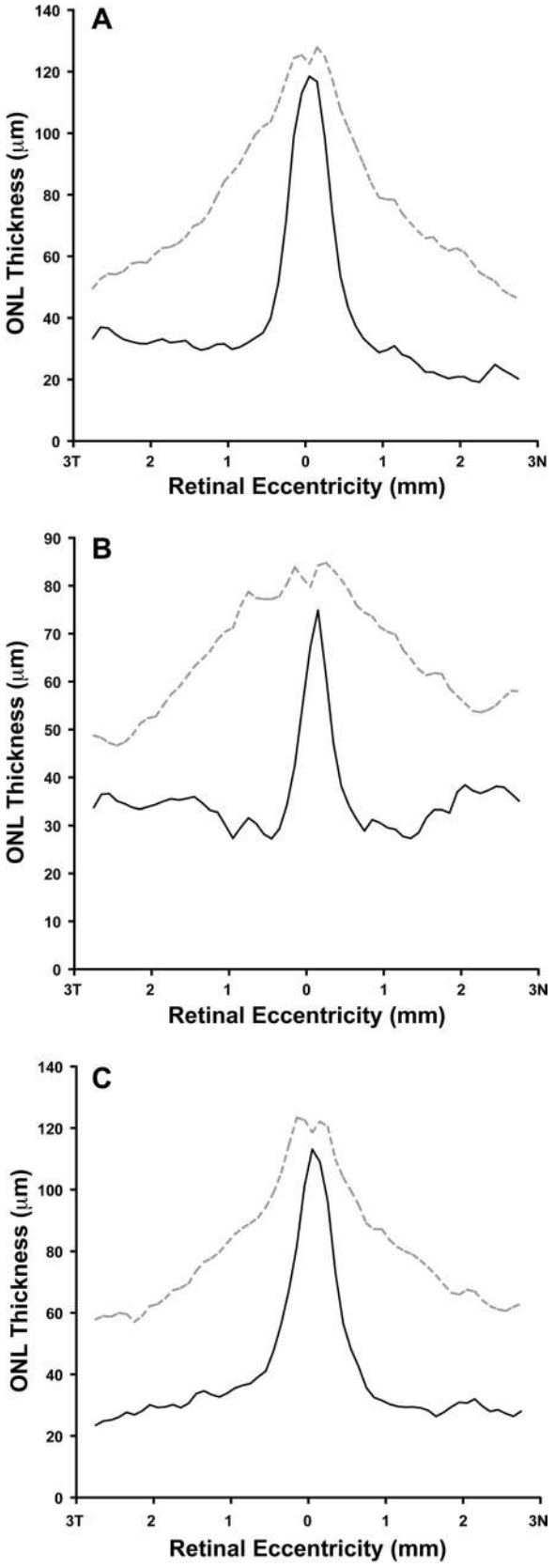

FIGURE 4. Manual segmentations demonstrating the difference in retinal thickness at each eccentricity along a single horizontal B-scan in three subjects imaged on the Bioptigen SD-OCT. *Dashed gray lines*: thickness measurements of the ONL using existing measurements of thickness between the ELM and the OPL. *Solid black line*: true measurement of the ONL after removal of HFL.

creased as scan angle decreased, which corresponded to temporal displacement. In two patients there was a fall-off of relative intensity of the nasal HFL after 9°. Conversely, as scan angle increased, reflectivity of the temporal macula increased. There was no resultant fall-off for the temporal retina, with maximum relative intensity obtained at 6°.

Measurements of HFL thickness as a percentage of the total thickness between the ELM and the OPL was performed when HFL intensity was in the hyporeflective state, which offered a clearer visualization of the transition between HFL and OPL. HFL accounted for an average 58% ± 3% of this thickness at a position 1 mm away from the foveal center in these eyes, with no significant difference between nasal and temporal HFL.

Manual segmentation of HFL along the entire extent of single-averaged B-scans obtained with Bioptigen in three subjects illustrated the difference between measurements of the entire thickness between the ELM and the OPL compared with the thickness of the ONL alone with the exclusion of HFL (Fig. 4). True ONL area represented 50%, 55%, and 49% of the area measured using the entire ELM to OPL space in subjects A, B, and C, respectively.

Two patients imaged with Bioptigen, each with macular pathology deforming the RPE and overlying retinal structures, were retrospectively identified. The first patient had a dome-like pigment epithelial detachment from central serous retinopathy (CSR). The second patient had age-related macular degeneration (AMD) with drusen causing an elevation of the RPE. Both of these pathologies had the effect of altering the angle at which HFL lies relative to the pupil. Variable reflectivity was evident in the anatomic space corresponding to HFL (Fig. 5), which appeared hyporeflective on the up-sloping aspect of the lesions closest to the foveal center while appearing hyperreflective on the down-sloping aspect of the pathology away from the foveal center. Two patients with macular pathology from CSR and AMD were also imaged dynamically using Cirrus. Significant changes in HFL intensity were observed at each SD-OCT beam entry position but were most striking at the extremes of the horizontal entry positions (Fig. 6).

DISCUSSION

In vivo cross-sectional retinal anatomy and pathology as visualized by OCT has revolutionized the study of retinal disease. Since its original commercial deployment, OCT technology has become much faster, has an improved axial resolution, and has incorporated frame-averaging software capable of increasing the signal-to-noise ratio. Although these advances have allowed additional layers to be resolved, particularly in the outer retina, they do not routinely visualize HFL as distinct from the ONL. However, the *optical* contrast necessary to visualize this layer can be brought out by altering the angle of the OCT entry beam on HFL, which consequently alters its reflectivity relative to the ONL. Thus, in addition to the technology used to generate a scan, the technique in which the OCT data are collected can directly determine what is visualized. Future software could allow registration of images acquired at different pupil entry positions to provide the clearest overall delineation of HFL from the ONL across an entire B-scan.

We observed that as the SD-OCT entrance beam moved closer to the edge of a dilated pupil, the reflectivity of HFL on that side of the fovea was reduced whereas HFL reflectivity on the opposite side of the fovea increased. Because the intensity

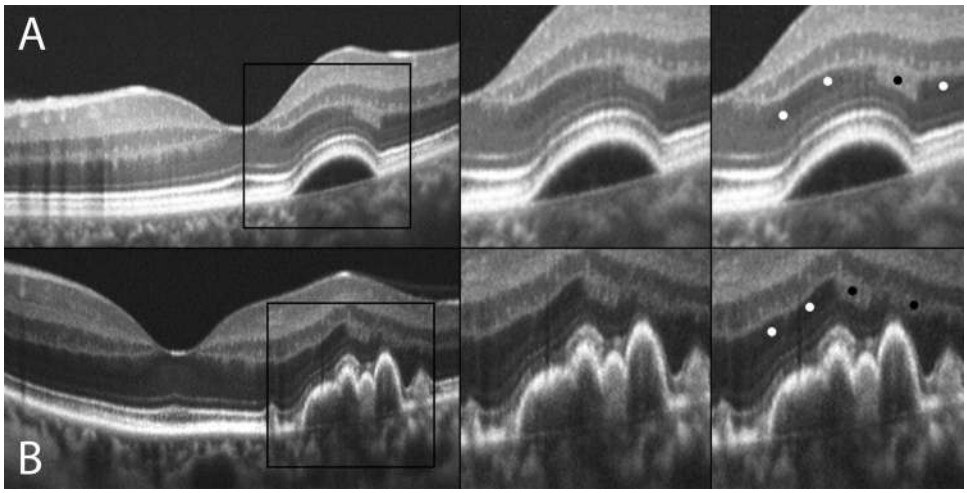

FIGURE 5. Clinical visualization of reflectivity changes in HFL. (**A**) Central serous chorioretinopathy. Immediately above the serous pigment epithelial detachment, HFL reflectivity varies from hyporeflective (*white dots*) to hyperreflective (*black dots*) based on the RPE geometry altering the orientation of HFL. Note the changes in the IS/OS junction reflectivity and the homogeneous reflectivity of the IPL. (**B**) Nonexudative (dry) AMD. Because of drusen there is RPE elevation that alters the orientation of HFL and produces similar hyporeflective and hyperreflective segments.

of reflected light varies with pupil entry position, HFL exhibits directional reflectance. We confirmed this finding was a consistent effect using a variety of scan protocols, multiple subjects, and two separate commercially available SD-OCT systems. We found this effect to be accentuated by, but not dependent on, the use of frame averaging to reduce speckle noise.

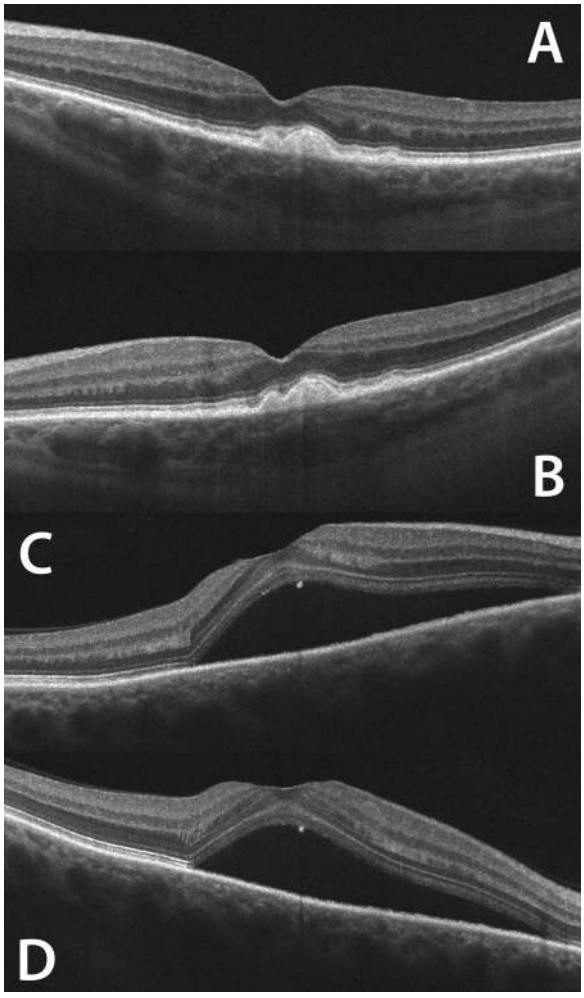

FIGURE 6. Clinical examples of the effect of beam entry position on the reflectivity visible in HFL. (**A**) HFL temporal to drusen appears hyperreflective when acquired with a nasal beam entry. (**B**) Temporal beam entry alters this intensity significantly. (**C**, **D**) Variation in HFL intensity is seen to vary with beam position in this patient with subretinal fluid from central serous retinopathy.

Accompanying this directional reflectance is the apparent tilt of the B-scan. This is "apparent" in that the real geometry of the eye does not change when using an eccentric entry position of the SD-OCT beam, but the optical path lengths of the scan do change. We found that the pupil entry position by which the SD-OCT B-scan appeared flat varied between subjects and did not necessarily correspond the geometric center of the pupil. However, once that position was identified, there was a predictable effect achieved by movement of the OCT entry beam. As the SD-OCT beam is moved nasally, the distance light must travel to and from the nasal macula is shorter than the path it must take to and from the temporal retina. The resultant B-scan is consequently tilted in appearance. The degree of this tilt served as an indirect means to calculate the entry beam position relative to the scan direction and was directly related to the relative reflectivity of HFL when normalized by the IPL in all subjects analyzed. The IPL was found to be relatively invariant in reflectivity at each of the eccentricities and, accordingly, served as a control for the directionally reflective HFL. Although HFL intensity varied without this normalization, normalization isolated the effects of directional reflectance from the overall image intensity variation induced by other pupil position–dependent changes, such as variable ocular transmission and scatter.

Directional reflectivity is a property shared by several retinal structures in which the optical principles behind their occurrences are well understood. For example, in photoreceptor IS and OS, the optical Stiles-Crawford effect[22] exists because of photoreceptors acting as waveguides, each directed at the center of the pupil. Additionally, the surface reflection visualized from the ILM in young eyes is caused by specular reflection from the smooth interface between two media of different refractive indices.

The directional reflectivity of the retinal nerve fiber layer (RNFL) has been well characterized by in vitro experiments.[23,24] The conclusion of these experiments was that a ray of light incident on the RNFL scatters into a conical sheet coaxial to the fiber bundle with the same angle relative to the fibers as the incident ray. Based on this experimental evidence, reflectivity of the human RNFL was modeled as light scattering by cylinders, and the implications of variability caused by directional reflectance on clinical measurements was discussed.[25] The mechanism of the directional reflectivity displayed by HFL was most consistent with that of the RNFL

because both these structures are composed of long cylindrical axons. The magnitude of the change in HFL reflectivity we observed because of the change in beam position was also consistent with that observed for the RNFL in rat retina.[24]

However, the RNFL appeared highly reflective when imaged through the center of the pupil until it turned to enter the optic canal, whereas HFL did not. This difference can be explained by the oblique orientation of HFL, which was due to axons running from photoreceptor nuclei toward the horizontally displaced cells of the inner retina. As the beam was displaced eccentrically in the pupil, the angle at which these light rays were incident on HFL changed, and consequently, so did their primary scattering angle. As the angle of incidence approached normal to HFL, increasingly more light was scattered back from this layer to escape the pupil and be visualized as OCT hyperreflectivity. Alternatively, with shallower angles of incidence, light scattered further away from the exit pupil, creating a hyporeflective HFL on SD-OCT (Fig. 7).

Quantitative estimates suggest results that are consistent with our observations. Using the Bennett-Rabbetts' model eye,[26] the approximate angle of incidence of light rays emanating from an entry position 3 mm from the anatomic axis was calculated to be approximately 8.5° to the retina. The angle of HFL in Figure 1 was calculated to be approximately 8°. These estimates predict that on the side of the fovea opposite the pupil entry position, light would be incident on HFL nearly normal to the axon orientation, resulting in maximal reflectivity back toward the exit pupil. This was consistent with the data presented in Figure 3, showing maximal intensity of HFL occurred near 8°, and declined beyond that point nasally.

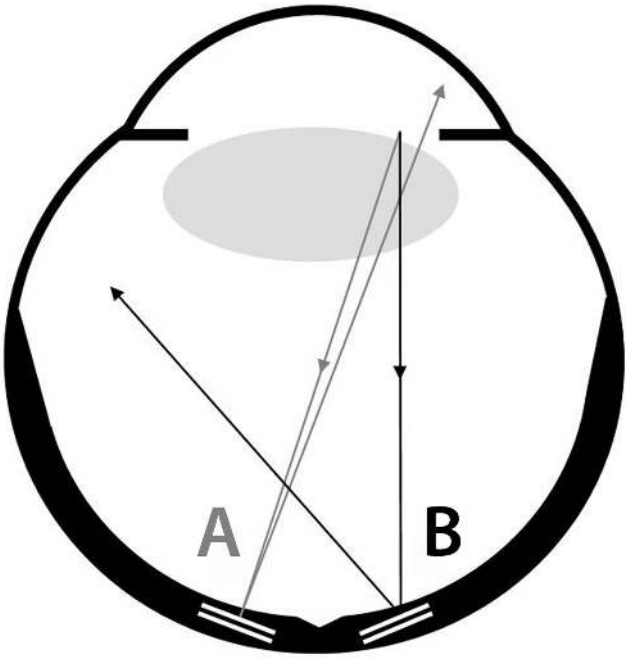

Figure 7. Unscaled schematic of HFL reflectivity through an eccentric pupil. Light rays from the edges of a B-scan centered on the fovea from an eccentric entry position are shown. These light rays encounter the obliquely oriented HFL (*white lines* within thickened retina) and scatter at an angle equal to its angle of incidence. A light ray along path A (*gray line*) scatters back from HFL close to the normal and back through the pupil to produce a hyperreflective HFL. However, a light ray along path B (*black*) scatters toward the opposite side of the eye without exiting the pupil and consequently appears hyporeflective on a corresponding B-scan. Note path A is longer than path B, accounting for the tilt of the B-scans in Figure 2.

Again consistent with our data, this model predicts that light rays would encounter HFL on the same side of the fovea as the entry beam at an angle of incidence around 17°, resulting in a reflection directed away from the exit pupil and appearing hyporeflective on OCT.

Recognition of the optical principles governing HFL reflectivity provides an explanation for the "unexpected" reflectivity in this layer because of pathology that affects the retinal geometry. The images in Figures 5 and 6 demonstrate reflectivity changes caused by alterations in the normal geometry of the retina, where pigment epithelial detachment, drusen, or subretinal fluid alters the angle of the cone of light reflecting from HFL. Optical changes in HFL are introduced by these protuberances by elevating and changing the orientation of its fibers relative to the pupil such that different segments of HFL may appear to be hyporeflective and hyperreflective overlying a single deformation. Diffuse hyperreflectivity accompanying drusen has been commented on previously and has been theorized to represent a "degenerative cellular process."[19] Although this explanation is possible, the anatomic location of hyperreflectivity attributed to drusen in Figure 6 corresponds to HFL, and its intensity can be seen to vary substantially with pupil entry position, supporting the idea of an optical effect. Now that a means to visualize HFL has been recognized, similar types of pathology could be dynamically imaged to further distinguish optical alterations from independent pathologic processes.

Identification of the true dimensions of the ONL is critical to clinical studies that aim to accurately measure macular photoreceptor nuclei thickness without the confounding effect of HFL. Recognition of a means by which to optically section the previously homogeneously reflecting tissue located between the ELM and OPL affords this distinction. It is possible that the nuclear thinning reported by Schuman et al.[19] might have been an underestimate and that the segmentation of ONL and HFL independently would have further bolstered the importance of their measurements. For OCT data that have already been acquired, the ability to infer true photoreceptor thickness from histologic data will be useful but is limited. The heterogeneity evident in Figure 4 demonstrates that HFL thickness varies between persons and by eccentricity from the foveal center even in subjects with normal vision. This variability is expected given observed variation in foveal cone density[27] and foveal pit morphology.[28]

This study did not seek to convey average or normal values of the HFL and ONL thicknesses. Accurate reporting of normative data would depend on a much larger number of subjects and on several parameters that were not precisely measured in this study, including axial length and refractive error. Furthermore, it is unclear whether HFL intensity and thickness measurements 1 mm away from the foveal center are more important than measurements at other eccentricities. This location was selected as a convenient distance from which to measure because of the substantial contribution of HFL that was not confounded by vascular shadowing. Additionally, the choice of rectangle size used to measure the intensity of reflectivity was not necessarily optimal. However, the area was large enough to generate a reproducible distribution of values with a small SD, yet it was small enough to reliably fit within HFL and the IPL and was invariant to shifts of several pixels in any direction. Future studies can examine volumetric data in larger numbers of patients along all A-scans at eccentric entry positions to determine normative values of true ONL thickness and intensity visualized by SD-OCT.

The striking image quality achievable with SD-OCT systems makes it tempting to directly correlate retinal layers visualized with SD-OCT images with retinal histology. However, these are not identical; they vary based on the optical properties of

retinal tissue. Importantly, an SD-OCT image depends not only on the particular system used but on the technique by which an image is acquired. Revealing the directional reflectivity of HFL by altering the beam entry position is an example of this phenomenon and can be exploited to gain a more thorough understanding of the retina in health and disease.

Acknowledgments

The authors thank Jacque L. Duncan and Adam M. Dubis for technical assistance.

References

1. Hogan MJ, Alvarado J, Weddell J. *Histology of the Human Eye*. Philadelphia: WB Saunders Company; 1971.
2. Hendrickson AE, Yuodelis C. The morphological development of the human fovea. *Ophthalmology.* 1984;91:603–612.
3. Yuodelis C, Hendrickson A. A qualitative and quantitative analysis of the human fovea during development. *Vision Res.* 1986;26:847–855.
4. Drasdo N, Millican CL, Katholi CR, Curcio CA. The length of Henle fibers in the human retina and a model of ganglion receptive field density in the visual field. *Vision Res.* 2007;47:2901–2911.
5. Gass JDM. *Stereoscopic Atlas of Macular Diseases*. 3rd ed. St. Louis, MO: CV Mosby Company; 1987:746–751.
6. Hunter DG, Patel SN, Guyton DL. Automated detection of foveal fixation by use of retinal birefringence scanning. *Appl Opt.* 1999; 38:1273–1279.
7. Puliafito CA, Hee MR, Lin CP, et al. Imaging of macular diseases with optical coherence tomography. *Ophthalmology.* 1995;102: 217–229.
8. Sull AC, Vuong LN, Price LL, et al. Comparison of spectral/Fourier domain optical coherence tomography instruments for assessment of normal macular thickness. *Retina.* 2010;30:235–245.
9. Wojtkowski M, Leitgeb R, Kowalczyk A, Bajraszewski T, Fercher AF. In vivo human retinal imaging by Fourier domain optical coherence tomography. *J Biomed Opt.* 2002;7:457–463.
10. Jorgensen TM, Thomadsen J, Christensen U, Soliman W, Sander B. Enhancing the signal-to-noise ratio in ophthalmic optical coherence tomography by image registration–method and clinical examples. *J Biomed Opt.* 2007;12:041208.
11. Anger EM, Unterhuber A, Hermann B, et al. Ultrahigh resolution optical coherence tomography of the monkey fovea: identification of retinal sublayers by correlation with semithin histology sections. *Exp Eye Res.* 2004;78:1117–1125.
12. Ko TH, Fujimoto JG, Schuman JS, et al. Comparison of ultrahigh- and standard-resolution optical coherence tomography for imaging macular pathology. *Ophthalmology.* 2005;112:23.
13. Ergun E, Hermann B, Wirtitsch M, et al. Assessment of central visual function in Stargardt's disease/fundus flavimaculatus with ultrahigh-resolution optical coherence tomography. *Invest Ophthalmol Vis Sci.* 2005;46:310–316.
14. Matsumoto H, Sato T, Kishi S. Outer nuclear layer thickness at the fovea determines visual outcomes in resolved central serous chorioretinopathy. *Am J Ophthalmol.* 2009;148:105–110.
15. Christensen UC, Kroyer K, Thomadsen J, Jorgensen TM, la Cour M, Sander B. Normative data of outer photoreceptor layer thickness obtained by software image enhancing based on Stratus optical coherence tomography images. *Br J Ophthalmol.* 2008;92:800–805.
16. Bagci AM, Shahidi M, Ansari R, Blair M, Blair NP, Zelkha R. Thickness profiles of retinal layers by optical coherence tomography image segmentation. *Am J Ophthalmol.* 2008;146:679–687.
17. DeBuc DC, Somfai GM, Ranganathan S, Tatrai E, Ferencz M, Puliafito CA. Reliability and reproducibility of macular segmentation using a custom-built optical coherence tomography retinal image analysis software. *J Biomed Opt.* 2009;14:064023.
18. Rha J, Dubis AM, Wagner-Schuman M, et al. Spectral domain optical coherence tomography and adaptive optics: imaging photoreceptor layer morphology to interpret preclinical phenotypes. *Adv Exp Med Biol.* 2010;664:309–316.
19. Schuman SG, Koreishi AF, Farsiu S, Jung SH, Izatt JA, Toth CA. Photoreceptor layer thinning over drusen in eyes with age-related macular degeneration imaged in vivo with spectral-domain optical coherence tomography. *Ophthalmology.* 2009;116:488–496.
20. Byeon SH, Chu YK. Interpretation of fovea center morphologic features in optical coherence tomography. *Am J Ophthalmol.* 2009;148:474–475.
21. Tanna H, Dubis AM, Ayub N, et al. Retinal imaging using commercial broadband optical coherence tomography. *Br J Ophthalmol.* 2010;94:372–376.
22. Gao W, Cense B, Zhang Y, Jonnal RS, Miller DT. Measuring retinal contributions to the optical Stiles-Crawford effect with optical coherence tomography. *Opt Express.* 2008;16:6486–6501.
23. Knighton RW, Baverez C, Bhattacharya A. The directional reflectance of the retinal nerve fiber layer of the toad. *Invest Ophthalmol Vis Sci.* 1992;33:2603–2611.
24. Knighton RW, Huang XR. Directional and spectral reflectance of the rat retinal nerve fiber layer. *Invest Ophthalmol Vis Sci.* 1999; 40:639–647.
25. Knighton RW, Qian C. An optical model of the human retinal nerve fiber layer: implications of directional reflectance for variability of clinical measurements. *J Glaucoma.* 2000;9:56–62.
26. Bennet AG, Rabbetts RB. *Bennett and Rabbett's Clinical Visual Optics*. 3rd ed. Edinburgh, UK: Butterworth-Heinemann; 1998: 209–212.
27. Curcio CA, Sloan KR, Kalina RE, Hendrickson AE. Human photoreceptor topography. *J Comp Neurol.* 1990;292:497–523.
28. Dubis AM, McAllister JT, Carroll J. Reconstructing foveal pit morphology from optical coherence tomography imaging. *Br J Ophthalmol.* 2009;93:1223–1227.